Title: Printed miniature robotic actuators with curvature-induced stiffness control inspired by the insect wing

Author: Runni Wu,[1]* Kin Wa Kwan,[1] Alfonso Hing Wan Ngan[1]

Address: [1]Department of Mechanical Engineering, The University of Hong Kong, Pokfulam Road, Hong Kong, P.R. China

*Corresponding author, e-mail address: rnwu@connect.hku.hk

Keywords: Tunable stiffness, 3D printing, electrochemical actuator, transition metal oxide

Abstract: Stimuli-responsive actuating materials offer a promising way to power insect-scale robots, but a vast majority of these material systems are too soft for load bearing in different applications. While strategies for active stiffness control have been developed for humanoid-scale robots, for insect-scale counterparts for which compactness and functional complexity are essential requirements, these strategies are too bulky to be applicable. Here, we introduce a method whereby the same actuating material serves not only as the artificial muscles to power an insect-scale robot for load bearing, but also to increase the robot stiffness on-demand, by bending it to increase the second moment of area. This concept is biomimetically inspired by how insect wings stiffen themselves, and is realized here with manganese dioxide (MnO_2) as a high-performing electrochemical actuating material printed on metallized polycarbonate films as the robot bodies. Using an open-electrodeposition printing method, the robots can be rapidly fabricated in one single step in ~15 minutes, and they can be electrochemically actuated by a potential of ~1 V to produce large bending of ~500° in less than 5 s. With the stiffness enhancement method, fast (~5 s) and reversible stiffness tuning with a theoretical increment by ~4000 times is achieved in a micro-robotic arm at ultra-low potential input of ~ 1 V, resulting in an improvement in load-bearing capability by about 4 times from ~10 μN to ~41 μN.

1. Introduction

Recently, there has been keen interest in using stimuli-responsive actuating materials to power robots that are compact and bio-mimicking [*1, 2, 3*]. In this paradigm, a robot, often in the insect scale, can produce lively motions with complex functions via strategically positioning an actuating material at specific locations of the robot body [*4, 5*]. A popular strategy is by 3D printing of actuating materials [*6, 7*] – a research topic now known as "4D printing" – with examples including shape memory polymers and composite hydrogels [*8*]. Recently, transition-metal oxides have been developed as high-performing multi-stimuli driven actuating materials [*2, 3, 9, 10, 11*] and methods have been developed to print them "on-demand" onto soft substrates to produce intricate insect-scale robots [*12*]. Such systems are lightweight and have high flexibility for motions, but a drawback is that they have low stiffness that decreases the load-bearing capability and therefore applicability.

For larger robotic devices, some strategies have been proposed to tune the stiffness of soft robots, although the applicability of these methods to insect-scale robots requiring high compactness and complex functionality is limited. Humanoid-scale robots can be stiffened by means of using granular media [*13*] or laminar strips [*14*], but then an external vacuum-production system is needed to switch between the compliant and rigid states which is too complex and bulky to be used for insect-scale robots. Shape-memory materials [*15, 16, 17*], thermo-rheological fluids as low-melting materials [*18, 19*] or magnetorheological fluids [*20*] can also be used to vary the robotic stiffness, but the stimuli required would be environmental heat or magnetic field which also requires bulky system designs. Light-driven systems have also been developed, including using thermally-expanding paraffin wax with the heat input delivered by carbon-nanotubes via a photothermal effect, but in this case the self-stiffening is coupled to the actuation [*21*]. Some strategies for tuning stiffness in response to electrical signals, which are convenient stimuli for insect-scale robots, have also been proposed [*22, 23, 24*]. These include the use of shape-memory polymers with the temperature input provided by

joule heating [*23*] and electro-active polymers (EAP) [*24*], but for the former the switching frequencies may be limited by the slow cooling process, and for the latter ultra-high driving potentials in kilovolts would be needed. Furthermore, most of the above strategies are only for controlling the structural stiffness function without motions delivered [*15*, *16*, *17*, *18*, *19*, *20*, *23*, *24*]. For small-scale robotic devices, strategies for stiffness tuning as well as actuation in response to electrical signals have also been proposed, including the use of oxygen-group functionalized graphene that exhibits a modulus increment during its tension actuation via thermal expansion by joule heating [*25*], and intracellular pressure tuning by reversible osmosis triggered by potential-driven electrolytic changes [*26*], in a synthetic system that bio-mimics the movement of plants [*27*]. However, in both cases, the stiffening is intrinsically coupled to the actuation straining rather than being independently controllable, and in the case of reversible osmosis, the response is very slow in minutes [*26*].

Here, we introduce a simple, 3D printing strategy to rapidly switch the stiffness of thin-film robots on-demand. Inspired by the biomimetic design of insect wings [*28*], a concept of "curvature-induced rigidity" is proposed (Figure 4a) by imposing a transversal curvature to stiffen a thin sheet against an external bending force [*29*, *30*]. With a versatile open-electrodeposition printing method for the oxide-based actuating material, the actuators can be quickly fabricated in typically less than 15 minutes, and in operation they can deliver fast and large bending over 500° within 5 s under an electrochemical potential of <1 V. Beside simple bending, foldable actuators, an independently controlled gripper and a micro-robotic arm with rapidly tunable stiffness are demonstrated. Compared to 4D printed actuators based on hydrogels or shape memory polymers [*8*], our actuators can produce fast, large, flexible and reversible shape transformation with much quicker stiffness tuning, in a simple structure fabricated by a simple one-step method. Compared to other systems in which the stiffening is intrinsically coupled with the actuation [*21*, *25*, *26*], the stiffening in our method is decoupled from the actuation, and the two are independently controllable.

2. Experimental Methods

Printed MnO_2 actuating layers. An open-electrodeposition printing setup [*31*], shown in Figure 1a, was used to print the MnO_2 actuating layers. A conductive syringe needle (of 3 ml syringe capacity and 1.27 mm needle external diameter) controlled by an *x-y-z* motion table was used to deliver a small droplet (~ 0.05 ml) of the electrodeposition electrolyte (0.1 M $C_4H_6MnO_4{\cdot}4H_2O$ and 0.1 M Na_2SO_4 [*12*]) at a small gap (~ 2 mm) maintained between the needle tip and a metallized substrate, and then the active material of MnO_2 was electrochemically formed within the gap via the application of a constant potential difference (1.8 V to 2.5 V with electrochemical workstation: CS350, Corrtest) between the syringe needle which acted as the reference electrode (RE) and the counter electrode (CE), and the substrate which acted as the working electrode (WE) [*31*]. In this work, the substrates used were a type of 10 μm thick micro-porous PC films (Nuclepore Track-Etched Polycarbonate Membranes, Whatman®) metallized by Au sputtering (Bal-tec SCD 005 Sputter Coater) beforehand. The micro-pores on the PC substrates allowed MnO_2 to be grown into them during electrodeposition, thus forming "micro-rivets" to enhance the adhesion between the MnO_2 layer and the substrate [*12*], as shown in Figure 1c. The printing was performed by moving the syringe needle at a speed of 1 to 500 mm/min. To achieve thicker active layers of MnO_2, the writing was conducted by repeatedly scanning over the same area, for which the average printing time per unit net printed length was measured. For the actuating hinges, the average printing time was 2.4 min/mm, and for the stiffness-enhancing hinges, the average printing time was 0.6 min/mm. (see Figure 4b). For the independent controlled gripper, muscle groups of the MnO_2 material were printed onto isolated Au-sputtered PC areas, which were then individually connected to a multi-control switch and triggered in 1 M Na_2SO_4 solution. Printed MnO_2 was characterized by scanning electron microscopy (SEM) in a Hitachi S-4800 microscope, and transmission electron microscopy (TEM) in an FEI Tecnai G20 Scanning TEM.

3. Results and discussion

3.1. Characterization and printed actuating behavior

Scanning electron microscopy (SEM) and transmission electron microscopy (TEM) examination (Figure 1b) show that the printed MnO_2 was amorphous and turbostratic [*11*] with a relatively crumpled microstructure. As mentioned above, MnO_2 was grown into the micro-pores of the PC film to form micro-rivets to enhance the adhesion between the MnO_2 actuating layer and the PC substrate film (Figure 1c) [*12*]. The electrochemical actuation in 1 M Na_2SO_4 electrolyte, as shown in Figure 1d, was due to a volume expansion accompanying Na^+ insertion to form MnOONa in the reduction process, and contraction accompanying recovery to MnO_2 under oxidation, during a reversible redox reaction (Figure 1d) [*32*]. Figures 1e-g show the effects of the applied constant potential, print-head speed, and the average printing time per line length on repeated scanning, on the actuation performance of the printed actuator. Figure 1e shows that the MnO_2 can only be printed effectively onto the conductive substrate with a printing potential of above ~1.9 V, indicative of a minimum potential threshold for the electrodeposition to happen. An constant potential of around 2.1 ~ 2.3 V applied resulted in relatively good actuating performance; although a larger potential may result in a thicker actuating layer because of the faster deposition in a certain time, rough and convex structures may also be resulted because of the faster deposition at the center of the locally printed feature [*33*], which may then produce decreased or uneven motions during the subsequent actuation. As shown in Figure 1f, a print-head speed of around 5 ~ 50 mm/min resulted in better actuating performance, and faster or lower speeds may not result in a relatively stable micro-electrolyte condition between the printing needle and the conductive substrate, and/or an even diffusion condition for the electrolyte along the printing path. Under a print-head speed of 5 mm/min, for a 1 cm long and ~ 1 mm wide actuating layer that was reversibly scanned for one cycle, the average printing time was ~ 2/(5mm/min) = 0.4 min/mm along the printing track; from the data in Figure 1g, the average deposition rate was ~1.6 to 2.2×10^4 $\mu m^3/s$ which is fast compared to other materials printed by the same open-electrodeposition method [*33*, *34*]. The local actuation

curvature can be increased by thickening the actuating layer, which can be achieved by reversibly scanning over the same printed area during electrodeposition (Figure 1g). However, when the thickness of actuating layer surpassed 4 μm, the actuating performance decreased, which may be due to the larger cracks formed in thicker actuating layers [*10*].

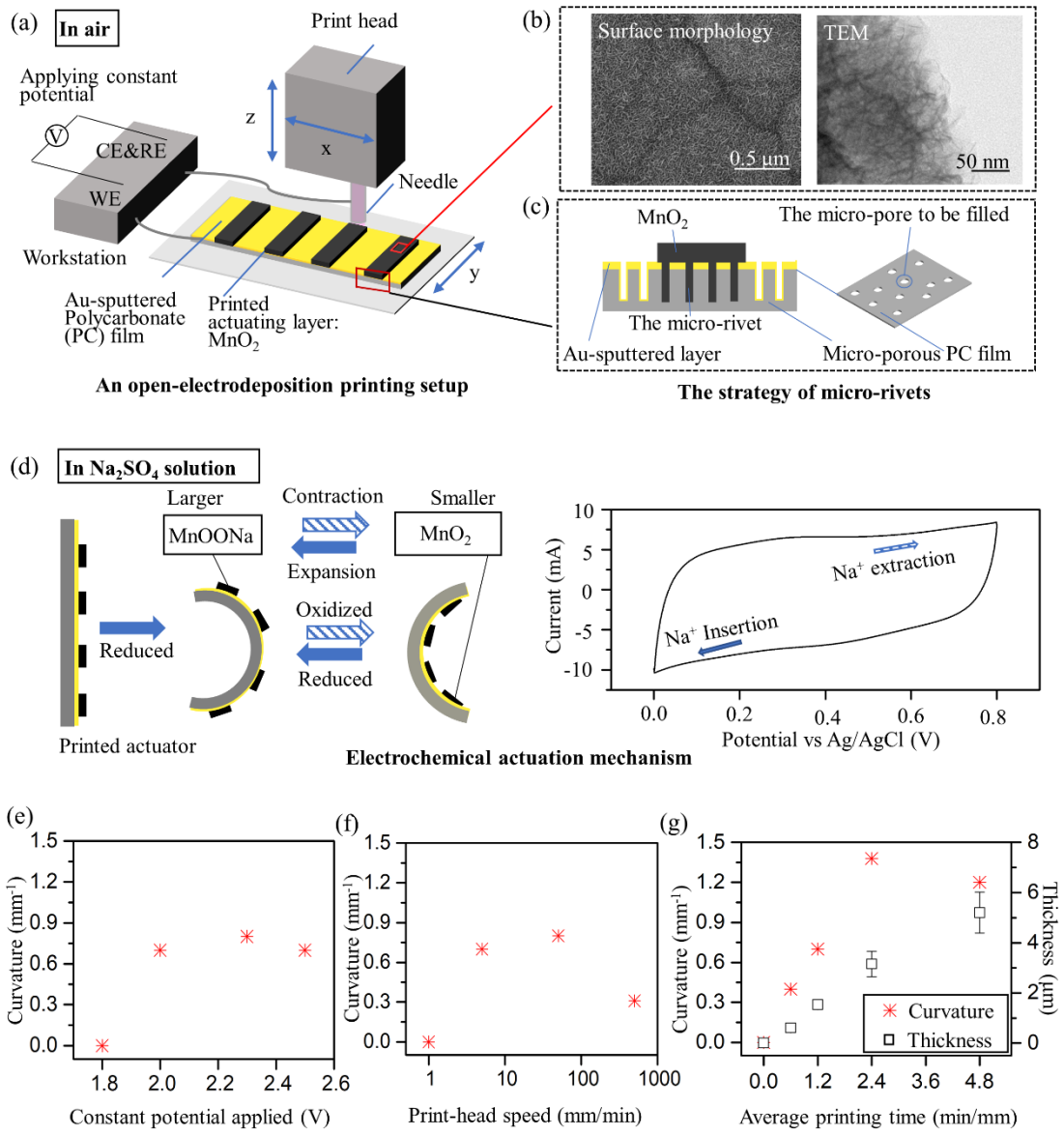

Figure 1. Characterization of the printed MnO_2 active layer. (a) Schematic of printing set-up. (b) SEM surface morphology and TEM of printed MnO_2 layer. (c) Schematic of the "micro-riveting" strategy for enhancing the adhesion between the printed MnO_2 layer and the PC film. (d) Schematic of actuating mechanism and corresponding cyclic voltammetry of the printed MnO_2 layer in 1 M Na_2SO_4 electrolyte with potential window of 0.0 V to 0.8 V at scan rate of 25 mV/s. (e~g) Dependence of actuating curvature of MnO_2 layers on printing parameters including (e) constant potential applied (at print-head speed of 5 mm/min for three cycle of forth and back scanning), (f) print-head speed (at step potential of 2.1 V for three cycle of forth and back scanning), and (g) average printing time per printed line length on repeated scanning for different cycles (at step potential of 2.1 V and print-head speed of 5 mm/min).

3.2. Foldable, sizable and independently controlled motions

Using the local printing method described above, both sides of the substrate can be printed, as shown in Figure 2a. Compared to one-side printing (Figure 2b), the two-side printing offers more applications in origami structures, in which mountain and valley self-folding hinges can deform the substrate in opposite directions in response to a simultaneous stimulus. The open-electrochemical printing method also breaks the limit of the traditional bath-electrodeposition method, in which large substrates can only be printed upon in a larger cell, which would then lead to uneven electrodeposition. Figure 2c shows a printed actuator over 5 cm long that exhibited a high actuating performance of curling into multiple loops, demonstrating that rather large and highly functional actuators can be printed by the present open-electrochemical printing method (supporting Movie S1). A gripper was further designed and printed for carrying out the typical robotic task of gripping (Figure 2d). Here, each actuator was connected to a multi-control switch, which allowed the rapid switching between different potential windows to tune the actuation speed and deformation. Such flexibility allowed the gripper to grasp a free-shape object (Figure 2d and supporting Movie S2).

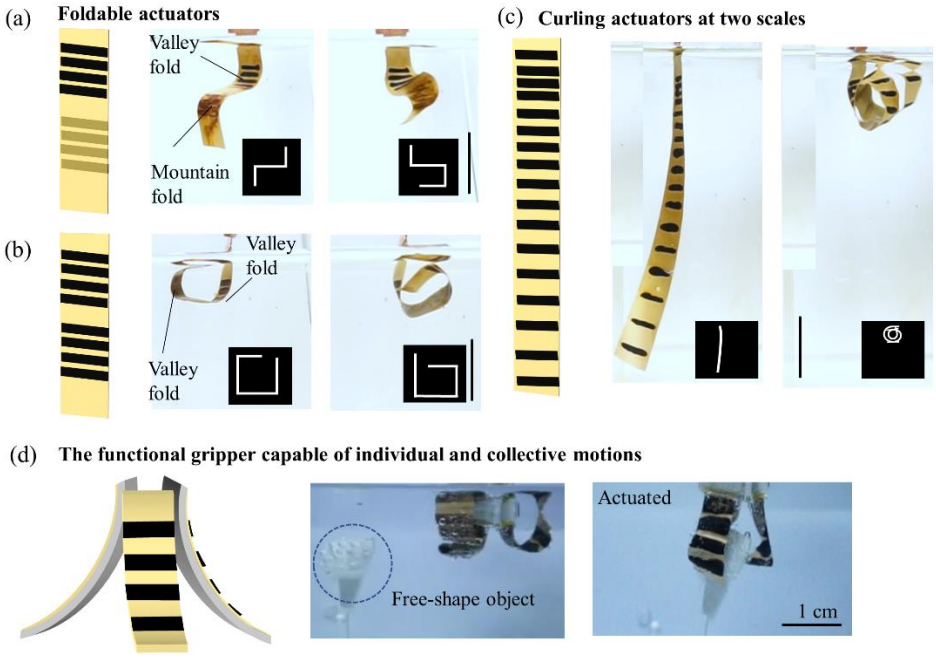

Figure 2. Complex motions by the printed MnO_2 hinges. (a~b) Foldable actuators enabled by two-side printing (scale bar: 1 cm). (c) An actuator over 5 cm long curling into loops (scale bar: 1 cm, see supporting video S1). (d) Functional gripper grasping a free-shape object (see supporting video S2).

3.3. Film-actuator with rapidly tunable stiffness

The thin passive layer would enable a large local curvature [*12*], but as shown in Figure 3, the intrinsic softness of a thin film would make the motion of the actuator hard to control effectively and lower the load-bearing capability. As shown in Figure 3a, large actuation at the elbow can be delivered by the printed actuating hinges, but the arm deforms significantly due to its gravitional load during the actuation process. Finite element method (FEM) (ABAQUS, Dassault Systèmes) simulation in Figure 3b also shows significant bending of the over-hanging passive layer (supposed to be the robotic arm) due to its own weight, despite the large actuation produced by the actuating hinges at the elbow.

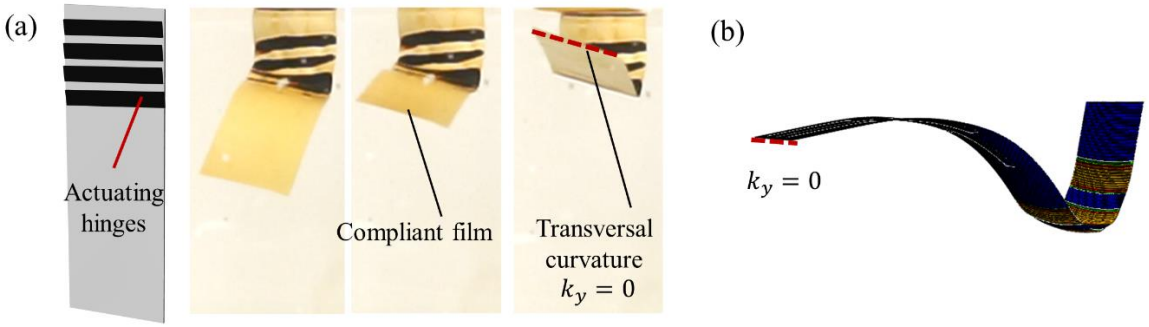

Figure 3. Compliant micro-robotic arm without curvature-induced rigidity. (a) Experimental and (b) FEM results.

Contrary to the above, dragonfly's wing is very thin (< 10 μm) but is capable of withstanding large loads by vurtue of a corrugated structure that produces stiffening [*28*]. This effect is also found in the beetle's hind wing [*35*], where the camber of the wing could stiffen itself. Figure 4a shows the stiffness-enhancement concept in such cases: for an elastic strip, formation of a curvature (k) about the long axis at the free end will enable the strip to endure its gravitional load, and increasing the curvature can rigidify the strip against the weight (g) better (Figure 4a) [*29*, *36*]. Inspired by the intelligence of insect wings, in our present thin-film based actuators, the curvature k_y for increasing rigidity was produced by another set of MnO_2 active hinges printed along the long axis of the film as shown in Figure 4b, in addition to the main MnO_2 actuating hinges that were printed in the transverse direction for the bending actuation of the device. For a thin-film strip with original bending stiffness $S_0 = 4Ebh^3/L^3$

where E is Young's modulus, b is width, h is thickness and L is length, the change in stiffness (ΔS) due to transversal and longitudinal curvatures, k_y and k_x respectively, is given by [*29, 30*]

$$\frac{\Delta S}{S_0} = \frac{b^4}{60h^2}\left(k_y - \nu k_x\right)^2 \quad (1)$$

where ν is the Poisson ratio. When the other end of the strip is clamped as shown in Figure 4a, an extra coefficient of $e^{-c\frac{b}{L}}$ is involved:

$$\frac{\Delta S}{S_0} = \frac{b^4}{60h^2}\left(k_y - \nu k_x\right)^2 e^{-c\frac{b}{L}} \quad (2)$$

where c ≈ 3.078 [*29*].

Also, Figure 1g indicates that increasing the thickness of the actuating layer would in general result in a larger local curvature. The intrinsic actuating stress σ_a and strain ε_a of actuators made with different MnO_2 thickness were calculated using the Timoshenko strain-mismatch theory for bi-layers as shown in Figure 5a [*12*, *37*]. It can be seen that the intrinsic actuating stress σ_a of MnO_2 is fairly constant at about 13 ± 3 MPa in the range studied, but the actuating strain ε_a increases with the average printing time and hence the thickness of the actuating layer, which is understandable as the substrate thickness is a constant factor so a thicker active layer should actuate more. The experimentally derived data in Figure 5a was used as input to simulate the curvature-induced-rigidity effect by the FEM, so as to guide our experimental design of the robotic arm in Figure 4b. The simulation setup is shown in Figure 5b. The MnO_2 and PC film were modeled as purely elastic solids with Young's modulus of 35.3 GPa [*32*] and 1.5 GPa (by tensile test), respectively. The electrochemical actuation was modelled as a thermal contraction problem in the FEM – to reproduce the experimentally measured actuating strains in Figure 5a, the thicker actuating hinges, thinner stiffness-enhancing hinges, and the PC substrate were modelled as thermally contracting solids with linear thermal expansion coefficients of ~1 %, ~0.3% and zero, respectively, under a negative temperature change of 1 degree imposed. Perfect bonding was assumed between the printed MnO_2 actuating hinges and the PC membrane. Since the static equilibrium response instead of

dynamic behaviour was calculated, fluidic drag effects of the electrolyte were not considered, and buoyance was also neglected. As shown in Figure 3b, in the absence of stiffness-enhancing actuating hinges, the simulated transverse curvature k_y of the micro-robotic arm is zero as expected. With a group of stiffness-enhancing hinges (intrinsic actuating strain ~0.34%, thickness ~0.6 μm) added as shown in Figures 5b and 4c, the simulated curvature k_y is ~ 0.28 mm^{-1}. According to the simulation result, for the experimental design of a micro-robotic arm in Figure 4d, the stiffness-enhancing pattern was printed with an average printing time of ~ 0.6 min/mm (intrinsic actuating strain ~0.34%, thickness 0.6 μm) to deliver an approprite transverse curvature, and the thicker actuating hinges were printed with an average printing time of ~2.4 min/mm (intrinsic actuating strain ~1.2%, thickness 3.25 μm) to deliver large local deformation at the arm's elbow for load bearing. The experimental transverse curvature was measured to be about 0.26 mm^{-1}, in good aggrement with the simulation result.

Pieces of solid plasticine (density ~1.9 g/cm^3) of different weights were applied to test the load-bearing capablity of the whole micro-robotic arm. In this procedure, the actuating unit was first switched on to lift up the robotic arm, and then the plasticine was added bit by bit onto the free end of the robotic arm until the arm became low enough to let the plasticine load drop off from it. The maximum loads thus recorded were 10.3 μN and 40.5 μN after accouting for the buoyancy, without and with the stiffness-enhancement unit, respectively. The load-bearing capability of the robotic arm was also calculated by FEM – as shown in Figure 5b, a node at the tip of the actuator is constrained to zero displacement, and as the actuating hinges actuate, the force at the constrained node was calculated to be 11.5 μN and 35.7 μN, respectively, without and with the stiffness-enhancing hinges turned on. The FEM predictions therefore agree with the experimental results (see table in Figure 4e) within around 10%, which may be due to the slightly uneven deposition during the printing process.

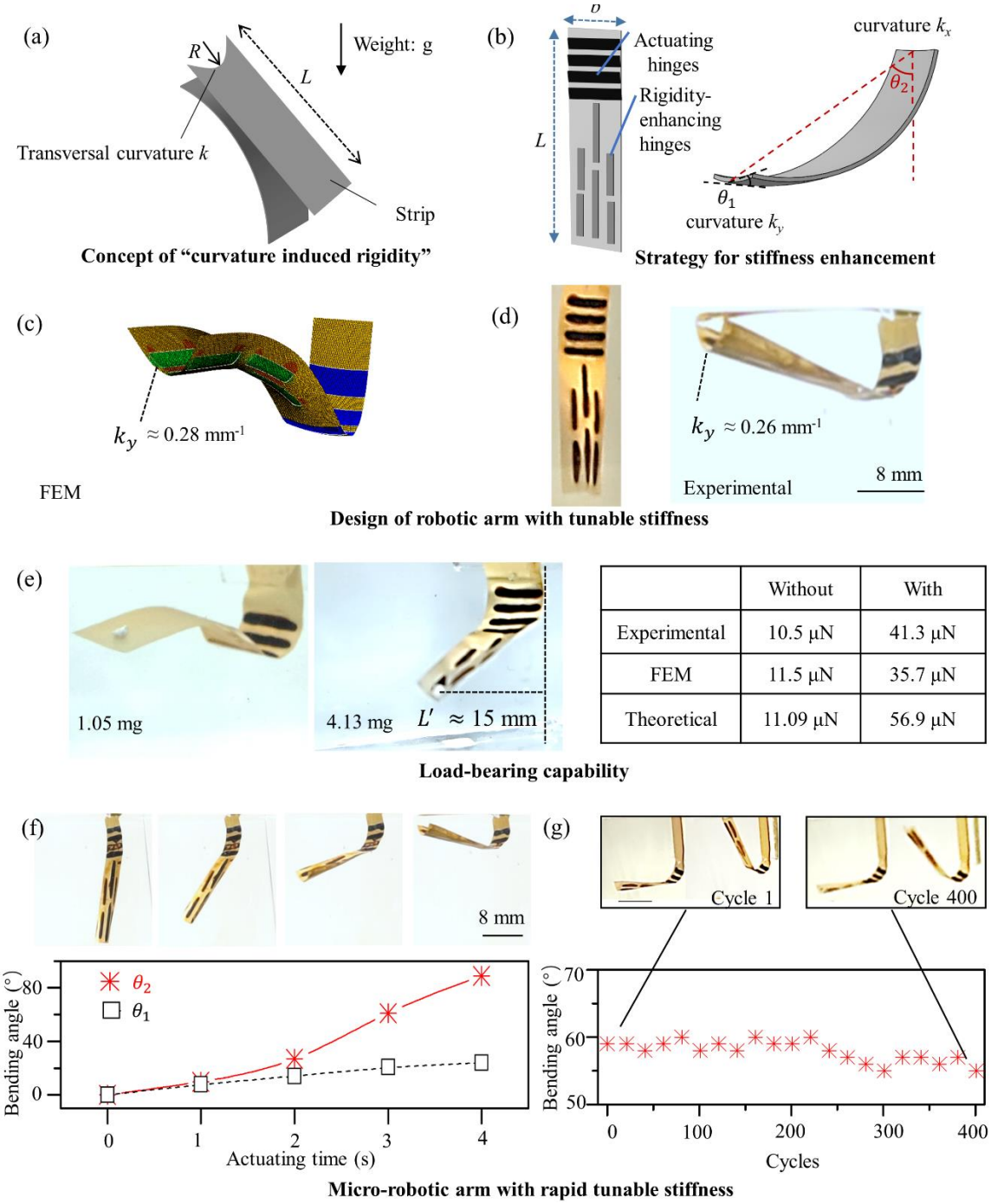

	Without	With
Experimental	10.5 μN	41.3 μN
FEM	11.5 μN	35.7 μN
Theoretical	11.09 μN	56.9 μN

Figure 4. Curvature-induced rigidity in a micro-robotic arm. (a) Concept of curvature-induced rigidity, with the stiffness of a strip enhanced by a transverse curvature *k* at the free end to increase the bearing capability of weight *(g)* [*29*, *36*]. (b) Schematic of the strategy for the printed actuator design comprising thick actuating hinges and thin stiffness-enhancing hinges, showing bending angles θ_1 and θ_2, and transverse and longitudinal curvatures k_y and k_x. (c) Finite element model and (d) experimental results of the rigidity-enhanced micro-robotic arm, with the intrinsic actuating strains for thinner and thicker actuating hinges being 0.34% and 1.25%. (e) Experimental, FEM and theoretical results for the load-bearing capability of the micro-robotic arm without and with stiffness-enhancement units. (f) Fast-responsive micro-robotic arm with real-time bending angles θ_1 and θ_2 (supporting Movie S3) and (g) good stability over ~ 400 cycles (scale bar: 1 cm).

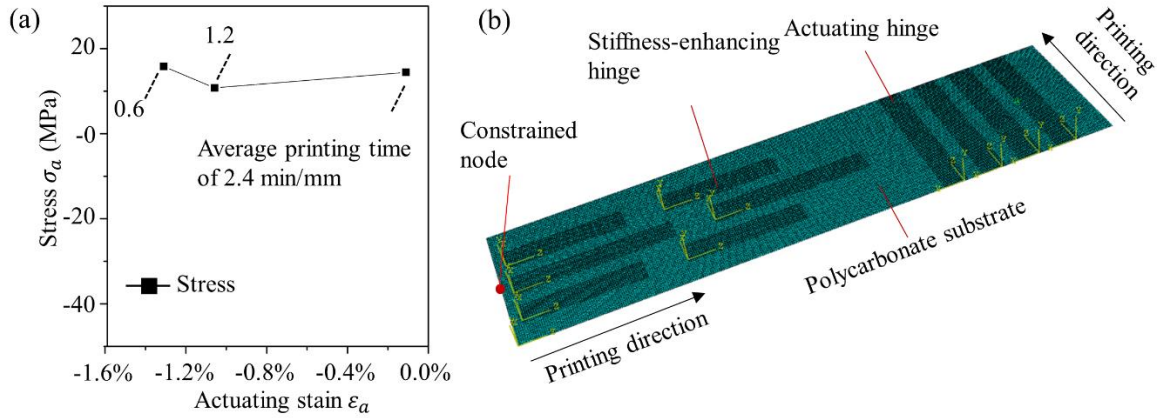

Figure 5. FEM simulation of load-bearing capability. (a) The intrinsic actuating stress and strain for the printed MnO_2 layers prepared from different average printing times. Actuating stress σ_a is calculated from the actuating curvature k_x via $\sigma_a = k_x/[6h_a(h_a+h_s)/(E_a h_a^3 + E_s h_s^3)]$, in which h_s = 10 μm, E_s = 1.5 GPa (by microtensile test), E_a = 35.3 GPa [*32*], and actuating strain is calculated from $\varepsilon_a = \left[\frac{1}{E_a} + \frac{h_a}{E_s h_s} + \frac{3h_a(h_a+h_s)^2}{E_a h_a^3 + E_s h_s^3}\right]\sigma_a$ [*12*]. (b) Geometry design of FEM for the actuating arm with stiffness-enhancing hinges. For the PC film, the length, width and thickness are 28 mm, 8 mm and 0.01 mm, respectively. For the actuating hinges, the length, width and thickness are 8 mm, 1.2 mm and 0.003 mm, and for the stifness-enhancement hinges, the length, width and thickness are 6~8 mm, 1.2 mm and 0.0006 mm. For calculating the load-bearing capacity, a node (marked red) is constrained to have zero displacement along the constrained direction, and as the actuating hinges actuate, the calculated forces at the constrained node along the constrained direction with and without the stiffness-enhancement units are 35.7 μN and 10.7 μN, respectively.

For the micro-robotic arm without the stiffness-enhancing unit, the load-bearing capability is limited by the intrinsic softness of the PC substrate. Here, adding the maximum sustainable weight of 10.3 μN was found to cause the substrate to deflect by Δx ~5 mm (Figure 6a). The intrinsic bending stiffness of the PC substrate calculated by $S_0 = 4Ebh^3/L^3$ is ~2.2 μN/mm, and for the deflection Δx of ~5 mm, the load is estimated to be ~5 × 2.2 = 11.0 μN (Figure 4e), in good agreement with the actual value of 10.3 μN. Experimentally, when the stiffness-enhancing unit was turned on, the arm portion of the robot became very rigid, as can be seen by the demonstration in Figure 6b, where a much-heavier plastine of dry weight ~ 700 mg before accouting for bouyance was used to push the micro-robotic arm downward. Here, after switching on the stiffness enhancing unit, the arm portion did not exhibit any noticeable deformation under the external load. Also, according to Equation (2), as the transversal curvature k_y is imposed the stiffness due to curvature-induced rigidity is increased to ~8.8 N/m.

At such a stiffness, an end-deflection of Δx = 5 mm as in Figure 6a would be produced by a load of ~ 44 mN, which is ~ 4000 times of the case without the stiffness-enhancers. Therefore, with the stiffness-enhancing unit in action, the load-bearing capability is limited by the intrinsic load-lifting capability of the actuating unit itself, since the arm portion would be close to rigid. Under no external load, the actuating unit was observed to produce a curvature k_x of 0.34mm^{-1} (Figure 6b). The bending moment of the actuating unit per unit width is given by $M = \frac{(E_a h_a^3 + E_s h_s^3) k_x}{12}$, where E_a and E_s are the Young's moduli of the active material and the substrate, and h_a and h_s are their thicknesses [*3*]. The maximum load capacity P_a of the robotic arm can be thought of as the load at the free end needed to straighten the actuating unit against its elasticity back to zero curvature, and hence $P_a \times L' = M \times b$ where the lever arm $L' \approx 15$ mm (see Figure 4e). The load-bearing capacity of the robotic arm, with the stiffness-enhancers in action, is then calculated to be P_a = 40.0 μN. As shown in Figure 4e, the theoretical load-bearing capacities with and without the stiffness enhancers are in good agreement with the experimental and FEM results.

As shown in Figure 4f, the micro-robotic arm with curvature-induced rigidity can be rapidly transformed in response to ultra-low voltage applied (~ 1V) within 5 seconds. The measured transverse folding angle θ_1 is larger at the free end than near the folding hinges, and as the bending energy is related to the transverse curvature, the small transverse curvature near the folding hinges is beneficial to the effective bending during the actuating motion. Finally, cyclic actuation tests were performed to evaluate the reliability of the printed micro-robotic arm, and as shown in Figure 4g, the robotic arm demonstrates stable actuation over at least 400 cycles without obvious degradation.

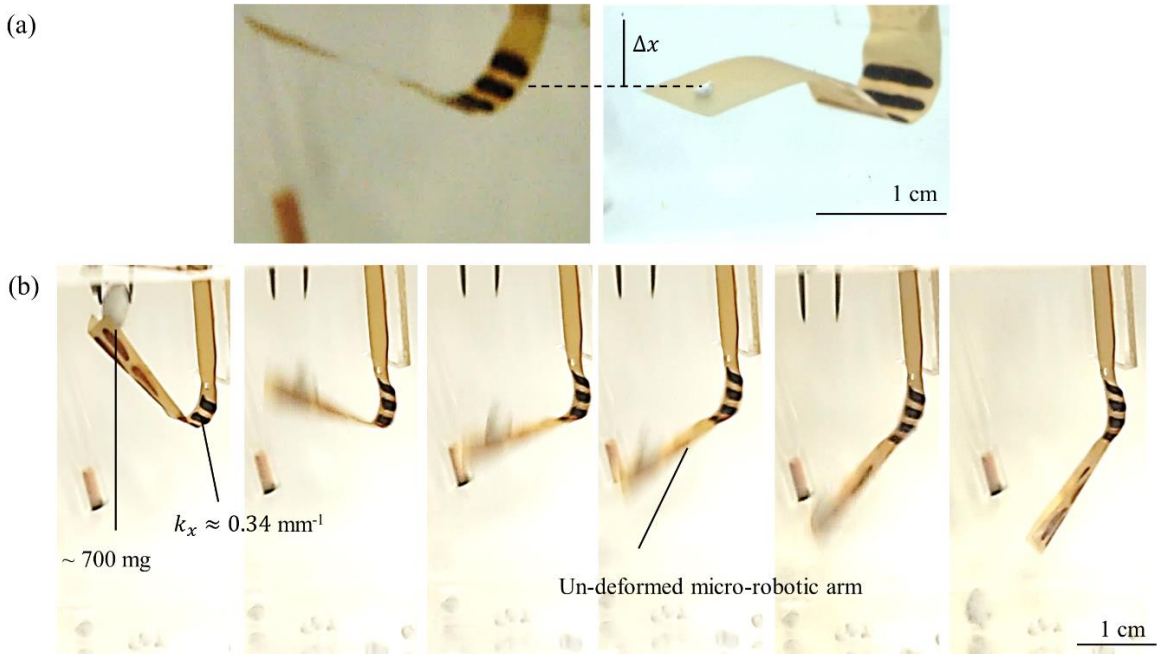

Figure 6. Comparison of robotic arm with and without stiffness-enhancing units. (a) Deflection Δx of the micro-robotic arm without the stiffness-enhancing units due to a load of 10.3 μN after accouting for buoyancy. (b) With the stiffness-enhancing units, the micro-robotic arm does not exhibit significant self-deformation under a load of ~330 mg after accouting for buoyancy.

4. Discussion

In this work, the critical problem of how to stiffen a thin-film robotic device in a fast, compact and easily controllable way was solved by a minimalist design concept of curvature-induced rigidity, in which a high-performing stimulus-responsive material is directly printed on pre-designed locations of the robot body to induce local curvatures to stiffen it. In particular, the high-performing, electrochemical actuating material of MnO_2 was employed as both the actuating muscles and the stiffness enhancers, leading to large actuation response with much improved load-bearing capability of the device, without sacrificing dexterity. Compared to the other stiffening strategies involving electrical stimuli (see Table 1), our actuating-stiffening method has the advantages of low electrical input (~ 1 V), fast response (~5 s), as well as uncoupled actuation and stiffening based on a single functional material driven by one type of stimuli. As for fabrication, existing methods for making metallic patterns include the selective-laser sintering [*38*], the ink-jet printing [*39*] or selective electrodeposition methods [*40*, *41*]. However, sintering is not suitable for the present type of active materials which are high-

melting oxides (MnO_2) or the substrate materials which are low-melting polymeric films, and the extra mask or the sacrificial layer involved in masked deposition methods may increase the cost and complexity of the fabrication process. On the other hand, the present printing fabrication method offers a great deal of flexibility in terms of the deposited materials, pattern geometry and thickness, thus allowing muscle and stiffening groups to be individually printed for independent electrical control, so that compact insect-scale robotic devices demonstrating complex motions and tunable stiffness can be easily fabricated. This printing method is applicable not only to the present MnO_2 material but also to other electrochemically printable actuating materials [*2*, *3*, *9*]. The motion of the resultant actuating device can be controlled by modifying the scan rate as well as the potential window applied during the printing of the actuating material. However, for effective electrochemical actuation of the present active material, the device must be submerged into the electrolyte instead of floating on it. Potential applications of the present actuating-stiffening concept may include marine (because of the role of Na^+ ions) biomimetic devices such as octopus-mimicking robots which require easy morphic changes of their bodies as well as the formation of temporary skeletons by self-stiffening [*22*].

Table 1 – Stiffness-tuning methods for insect-scale robots driven by electrical signals

Stiffening system	Input requirement	Response speed	Coupled with actuation	Other remarks
Shape memory polymers [*17*, *23*]	1.4 A [*17*]; 20~50 V [*23*];	Transition from solid to soft state is quick (in seconds), but reverse transition by cooling is slow	No. Actuation needs to separately provided (e.g., by a pneumatic system)	Complicated assembly process
Electroactive polymers [*24*]	kV range	Quick, less than 1 s	No. Tunable stiffness for structure only	-
Graphene functionalized with oxygen-rich groups [*25*]	~5 V	10 s	Coupled with actuation without independent control	Complicated preparation process
Reversible osmosis [*26*]	~1 V	Slow in minutes	Coupled with actuation without independent control	Biomimicking

Curvature-induced rigidity using printed stimuli-responsive materials (present work)	< 1 V	in ~ 5 sec	Based on same principle as actuation, but stiffening and actuation are separately controllable	Applicable to all types of stimuli-responsive materials that are printable

5. Conclusion

In summary, a versatile yet simple paradigm for fabricating micro-robots with fast response and independently controllable motions was established. By a low-cost desktop open-electrodeposition method, rapidly fabricated actuators capable of producing large, fast and complex motions in response to ultra-low electrochemical stimuli were demonstrated. Moreover, leveraging on the flexibility of the printing method, the actuating hinges not only rendered a motion-delivering function, but also a novel, on-demand structural stiffening function with a theoretical improvement of stiffness by ~4000 times. This study provides a simple technology for achieving self-stiffening as well as self-actuating functions for insect-scale thin-film structures.

Supporting Movies

Movie S1. A large-size curling actuator.

Movie S2. Functinoal gripper capable of grasping and manipulating the free-shape object.

Movie S3. The arm actuator with curvature-induced rigidity.

Author contributions: A.H.W.N. supervised the overall research. K.W.K. and R.W. conceptualized the printed MnO_2 actuator and curvature-induced actuating system. R.W. performed experiments and collected the data. R.W., K.W.K. and A.H.W.N. did the analysis and wrote the paper. **Funding:** The work is funded by the Kingboard Endowed Professorship in Materials Engineering at the University of Hong Kong. **Acknowledgements:** We thank Mr F.Y.F. Chan for help with TEM sample preparation and TEM operation. **Competing interests:** The authors declare that they have no competing interests.

References

1. Pieroni, M., Lagomarsini, C., De Rossi, D. & Carpi, F. Electrically tunable soft solid lens inspired by reptile and bird accommodation. *Bioinspiration and Biomimetics* **11**, 065003 (2016).
2. Kwan, K. W. *et al.* Light-stimulated actuators based on nickel hydroxide-oxyhydroxide. *Sci. Robot.* **3**, eaat4051 (2018).
3. Kwan, K. W. & Ngan, A. H. W. A high-performing, visible-light-driven actuating material responsive to ultralow light intensities. *Adv. Mater. Technol.* **4**, 1900746 (2019).
4. Wu, L. *et al.* Compact and low-cost humanoid hand powered by nylon artificial muscles. *Bioinspiration and Biomimetics* **12**, 026004 (2017).
5. Rogóż, M., Zeng, H., Xuan, C., Wiersma, D. S. & Wasylczyk, P. Light-Driven Soft Robot Mimics Caterpillar Locomotion in Natural Scale. *Adv. Opt. Mater.* **4**, 1689–1694 (2016).
6. Shafranek, R. T. *et al.* Stimuli-responsive materials in additive manufacturing. *Prog. Polym. Sci.* **93**, 36–67 (2019).
7. Ge, Q. *et al.* Multimaterial 4D Printing with Tailorable Shape Memory Polymers. *Sci. Rep.* **6**, 1–11 (2016).
8. Kuang, X. *et al.* Advances in 4D Printing: Materials and Applications. *Adv. Funct. Mater.* **29**, 1–23 (2019).
9. Kwan, K. W., Hau, N. Y., Feng, S. P. & Ngan, A. H. W. Electrochemical actuation of nickel hydroxide/oxyhydroxide at sub-volt voltages. *Sensors Actuators, B Chem.* **248**, 657–664 (2017).
10. Kwan, K. W. & Ngan, A. H. W. Visible-light-driven, nickel-doped cobalt oxides/hydroxides actuators with high stability. *ACS Appl. Mater. Interfaces* **12**, 30557–30564 (2020).

11. Ma, W., Kwan, K. W., Wu, R. & Ngan, A. H. W. High-performing, linearly controllable electrochemical actuation of c-disordered δ-MnO2/Ni actuators. *J. Mater. Chem. A* **9**, 6261–6273 (2021).
12. Wu, R., Kwan, K. W., Ma, W., Wang, P. & Ngan, A. H. W. Self-actuating origamis realized by independently printable and controllable stimuli-responsive creases. *Appl. Mater. Today* **20**, 100621 (2020).
13. Brown, E. *et al.* Universal robotic gripper based on the jamming of granular material. *Proc. Natl. Acad. Sci.* **107**, 18809–18814 (2010).
14. Narang, Y. S., Vlassak, J. J. & Howe, R. D. Mechanically Versatile Soft Machines through Laminar Jamming. *Adv. Funct. Mater.* **28**, 1707136 (2018).
15. Yang, Y., Chen, Y., Li, Y., Chen, M. Z. Q. & Wei, Y. Bioinspired robotic fingers based on pneumatic actuator and 3D printing of smart material. *Soft Robot.* **4**, 147–162 (2017).
16. Origamis, U. R., Firouzeh, A., Member, S., Salerno, M. & Paik, J. Stiffness Control With Shape Memory Polymer in underactuated robotic origamis. *IEEE Trans. Robot.* **33**, 765–777 (2017).
17. Zhang, Y. F. *et al.* Fast-Response, Stiffness-Tunable Soft Actuator by Hybrid Multimaterial 3D Printing. *Adv. Funct. Mater.* **29**, 1–9 (2019).
18. Cheng, N. *et al.* Design and analysis of a soft mobile robot composed of multiple thermally activated joints driven by a single actuator. *IEEE Internatinoal Conf. Robot. Autom.* 5207–5212 (2010).
19. Cheng, N. G., Gopinath, A., Wang, L., Iagnemma, K. & Hosoi, A. E. Thermally Tunable , Self-Healing Composites for Soft Robotic Applications. *Macromol. Mater. Eng.* **299**, 1279–1284 (2014).
20. Deshmukh, S. S. & Mckinley, G. H. Adaptive energy-absorbing materials using field-responsive fluid-impregnated. *Smart Mater. Struct.* **16**, 106–113 (2007).

21. Xu, L. *et al.* A Photoactuator Based on Stiffness-Variable Carbon Nanotube Nanocomposite Yarn. *ACS Appl. Mater. Interfaces* **12**, 40711–40718 (2020).
22. Manti, M., Cacucciolo, V. & Cianchetti, M. Stiffening in soft robotics: A review of the state of the art. *IEEE Robot. Autom. Mag.* **23**, 93–106 (2016).
23. Takashima, K. *et al.* Pneumatic artificial rubber muscle using shape-memory polymer sheet with embedded electrical heating wire. *Smart Mater. Struct.* **23**, 125005 (2014).
24. Carpi, F., Frediani, G., Gerboni, C., Gemignani, J. & De Rossi, D. Enabling variable-stiffness hand rehabilitation orthoses with dielectric elastomer transducers. *Med. Eng. Phys.* **36**, 205–211 (2014).
25. Dai, Z. *et al.* Hierarchical Graphene-Based Films with Dynamic Self-Stiffening for Biomimetic Artificial Muscle. *Adv. Funct. Mater.* **26**, 7003–7010 (2016).
26. Must, I., Sinibaldi, E. & Mazzolai, B. A variable-stiffness tendril-like soft robot based on reversible osmotic actuation. *Nat. Commun.* **10**, 1–8 (2019).
27. Kwan, K. W., Ye, Z. W., Chye, M. L. & Ngan, A. H. W. A mathematical model on water redistribution mechanism of the seismonastic movement of mimosa pudica. *Biophys. J.* **105**, 266–275 (2013).
28. Jang, J. H., Cho, K. & Yang, G. H. Design and Experimental Study of Dragonfly-Inspired Flexible Blade to Improve Safety of Drones. *IEEE Robot. Autom. Lett.* **4**, 4200–4207 (2019).
29. Pini, V. *et al.* How two-dimensional bending can extraordinarily stiffen thin sheets. *Sci. Rep.* **6**, 1–16 (2016).
30. Zhu, Y. *et al.* Manipulating three-dimensional bending to extraordinarily stiffen two-dimensional membranes by interference colors. *Nanoscale* **10**, 21782–21789 (2018).
31. Wang, P., Roberts, R. C. & Ngan, A. H. W. Direct microfabrication of oxide patterns by local electrodeposition of precisely positioned electrolyte: The case of Cu2O. *Sci. Rep.* **6**, 27423 (2016).

32. Liu, L. *et al.* The origin of electrochemical actuation of MnO2/Ni bilayer film derived by redox pseudocapacitive process. *Adv. Funct. Mater.* **29**, 1806776 (2019).
33. Chen, X., Liu, X., Childs, P., Brandon, N. & Wu, B. A low cost desktop electrochemical metal 3D printer. *Adv. Mater. Technol.* **2**, 1700148 (2017).
34. Seol, S. K. *et al.* Electrodeposition-based 3D Printing of Metallic Microarchitectures with Controlled Internal Structures. *Small* **11**, 3896–3902 (2015).
35. Ha, N. S., Truong, Q. T., Goo, N. S. & Park, H. C. Biomechanical properties of insect wings: The stress stiffening effects on the asymmetric bending of the Allomyrina dichotomabeetle's hind wing. *PLoS One* **8**, (2013).
36. Taffetani, M., Box, F., Neveu, A. & Vella, D. Limitations of curvature-induced rigidity: How a curved strip buckles under gravity. *EPL* **127**, 14001 (2019).
37. Ma, W., Kwan, K. W., Wu, R. & Ngan, A. H. W. Chemo-mechanical instability of light-induced humidity responsive bilayered actuators. *Extrem. Mech. Lett.* **39**, 100801 (2020).
38. Agarwala, M., David, B., Joseph, B., Harris, M. & Joel, B. Direct selective laser sintering of metals. *Rapid Prototyp. J.* **1**, 26–36 (1995).
39. Derby, B. & Reis, N. Inkjet Printing of Highly Loaded Particulate Suspensions. *MRS Bull.* **28**, 815–818 (2003).
40. Nagase, K., Kubo, S. & Nakagawa, M. Photochemically Grafted Polystyrene Layer Assisting Selective Au Electrodeposition. *Langmuir* **28**, 11646–11653 (2012).
41. Cho, S. H., Kim, S. H., Lee, J. G. & Lee, N. Micro-scale metallization of high aspect-ratio Cu and Au lines on flexible polyimide substrate by electroplating using SU-8 photoresist mask. *Microelectron. Eng.* **77**, 116–124 (2005).